Journal of Alloys and Compounds 1037 (2025) 182292

Contents lists available at ScienceDirect

Journal of Alloys and Compounds

journal homepage: www.elsevier.com/locate/jalcom

Effects of cationic substitution on the properties of $Sb_{1-x}Bi_xSeI$ (x = 0–1) compounds

Marc Dolcet Sadurni [a,*], Kristi Timmo [a], Valdek Mikli [a], Jüri Krustok [a], Mati Danilson [a], Artūras Suchodolskis [b], Cristian Radu [c,d], Amelia Elena Bocirnea [c], Aurelian Catalin Galca [c,e], Maarja Grossberg-Kuusk [a], Marit Kauk-Kuusik [a]

[a] Department of Materials and Environmental Technology, Tallinn University of Technology, Ehitajate Tee 5, Tallinn 19086, Estonia
[b] Department of Optoelectronics, Center for Physical Sciences and Technology, Sauletekio Av. 3, Vilnius 10257, Lithuania
[c] National Institute of Materials Physics, Atomistilor 405A, Magurele, Ilfov 077125, Romania
[d] Faculty of Physics, University of Bucharest, Atomistilor 405, Magurele, Ilfov 077125, Romania
[e] International Centre for Advanced Training and Research in Physics, Atomistilor 409, Magurele, Ilfov 077125, Romania

ARTICLE INFO

Keywords:
Antimony selenoiodide
Bismuth selenoiodide
Solid solution
Pnictogen chalcohalides

ABSTRACT

Pnictogen chalcohalide semiconductors are emerging materials with broad potential in energy-related applications, including solar cells, photocatalysis, photodetectors, batteries, supercapacitors, thermoelectric and piezoelectric generators. Their compositional flexibility allows fine tuning of structural and optoelectronic properties. In this study, microcrystalline powders of $Sb_{1-x}Bi_xSeI$ (x = 0–1) were synthesized from binary precursors by a solid-state method in evacuated quartz ampoules. Energy dispersive spectroscopy confirmed the successful substitution of Sb with Bi in $Sb_{1-x}Bi_xSeI$. The formation of solid solutions was also supported by Raman spectroscopy and X-ray diffraction (XRD). All materials exhibited needle-shaped crystal morphologies and orthorhombic crystal structure (*Pnma*), regardless of the Bi/Sb ratio. XRD patterns shifted toward smaller angles with increasing Bi content, indicating lattice expansion. Calculated lattice parameters (*b* and *c*) increased linearly with Bi incorporation, while the lattice parameter (*a*) remained constant. Raman spectra exhibited characteristic peaks at 182 cm^{-1} for Bi-Se vibration and 209 cm^{-1} for Sb-Se vibration, with intensity ratios reflecting Bi content. UV-Vis-NIR diffuse reflectance spectroscopy revealed a direct band gap that decreased from 1.7 eV (SbSeI) to 1.29 eV (BiSeI). Room-temperature photoluminescence measurements exhibited a single emission band, shifting from 1.75 eV to 1.41 eV with increasing Bi content. Ultraviolet photoelectron spectroscopy indicated a shift in the valence band maximum from 0.44 eV (SbSeI) to 1.1 eV (BiSeI). These findings highlight the tunability of $Sb_{1-x}Bi_xSeI$ compounds, offering pathways for optimizing their properties for specific optoelectronic applications.

1. Introduction

Heavy pnictogen chalcohalides are a recently rediscovered family of inorganic ternary semiconductors that are earth-abundant and non-toxic. These materials exhibit unique optoelectronic properties, such as ferroelectricity [1], high carrier mobilities, and strong anisotropic charge transport [2]. Due to their properties, pnictogen chalcohalides have attracted significant interest for use in photovoltaics [3–5] and other energy harvesting applications [6–9].

SbSeI and BiSeI share an orthorhombic crystal structure (space group *Pnma*) and exhibit a quasi-1D arrangement, consisting of aligned chains held together by weak van der Waals forces. This structural anisotropy enables efficient charge carrier transport along the chain axis, making them attractive for optoelectronic and thermoelectric applications [10]. SbSeI has a band gap energy of approximately 1.72 eV [11], while BiSeI exhibits a lower band gap of around 1.29 eV [12]. Although these materials are classified as indirect band gap semiconductors, the predicted difference between the direct and indirect band gaps is approximately ~0.2 eV for SbSeI [13] and ~0.1 eV for BiSeI [14]. Both materials also exhibit high absorption coefficients (~10^5 cm^{-1}) [15], supporting their potential for efficient light harvesting and energy conversion.

Advanced computational techniques have been used in several

* Corresponding author.
E-mail address: madolc@taltech.ee (M. Dolcet Sadurni).

https://doi.org/10.1016/j.jallcom.2025.182292
Received 15 May 2025; Received in revised form 2 July 2025; Accepted 15 July 2025
Available online 16 July 2025

theoretical studies of the electronic structure of SbSeI and BiSeI [13,14,16]. However, experimental investigations have thus far focused only on the band structure of SbSeI [17–20], with no experimental data reported for BiSeI. Understanding the band structure is crucial to selecting appropriate materials for photovoltaic applications. The optical band gap defines the theoretical efficiency limit of a solar cell, while appropriate band alignment with other cell layers is essential for achieving optimal device performance. According to the Shockley-Queisser (SQ) limit, the optimal band gap for a single-junction solar cell under AM1.5 G illumination is approximately 1.34 eV, corresponding to a theoretical maximum efficiency of around 33 % [21]. In multi-junction solar cells, wider band gaps are required to maximize efficiency across the solar spectrum [22]. For indoor photovoltaics (IPV), where artificial lighting such as white light emitting diodes (LEDs) is used, an optimal band gap of 1.7–1.9 eV is desired [23], making materials like SbSeI particularly promising for these applications. A viable strategy for tailoring the band gap of absorber materials is the synthesis of solid solutions from two parent compounds, enabling compositional optimization to achieve desired optoelectronic properties. Partial substitution of pnictogen cations [16,24–27], as well as chalcogen [28] and halide anions [29], has been demonstrated in various pnictogen chalcohalides. In the earlier study by Viskunets *et al.* [27], the formation of a continuous solid solution of $Sb_{1-x}Bi_xSeI$ with a step x = 0.1 was confirmed by XRD and differential thermal analysis (DTA), with all compositions crystallizing in an orthorhombic structure. Additionally, photoconductivity and optical absorption properties of these solid solutions were investigated in [26].

The present work aims to use $Sb_{1-x}Bi_xSeI$ solid solutions as absorber materials for various photovoltaic (PV) applications - from lower band gap compositions suitable for single-junction solar cells to wider band gaps tailored for tandem devices and IPV systems. However, while the tunable band gap (1.72–1.29 eV) makes these materials a promising and environmentally friendly candidate for next-generation energy harvesting technologies, further detailed analysis is still required.

In this study, $Sb_{1-x}Bi_xSeI$ (x = 0, 0.2, 0.4, 0.6, 0.8, and 1) solid solutions were synthesized by a solid-state reaction method to investigate the effect of Bi content on their structural, optical, and electronic properties. Increasing Bi content led to a nonlinear narrowing of the band gap, accompanied by a similar trend in the RT-PL peak emission energy and a transition in conductivity type. The relative intensity changes of the Sb–Se and Bi–Se Raman modes correlated with Bi content, enabling reliable estimation of metal composition in the solid solution using Raman spectroscopy. Changes in energy level alignment were also examined, and to the best of current knowledge, this study presents one of the first experimental band diagrams for the $Sb_{1-x}Bi_xSeI$ system.

2. Methodology

$Sb_{1-x}Bi_xSeI$ microcrystalline powders with different values of x (x = 0, 0.2, 0.4, 0.6, 0.8 and 1) were synthesized via a solid-state reaction route from self-prepared Sb_2Se_3 (5 N), Bi_2Se_3 (4 N), SbI_3 (3 N) and commercially available BiI_3 (Aldrich, 2 N). The masses of precursors containing Sb and Bi were calculated and weighed to achieve a total mass of 1 g with the desired Bi/Sb ratio, then mixed and ground in an agate mortar to ensure homogeneity and facilitate the reaction. The mixtures were poured into quartz ampoules (6.5 cm long, 1.2 cm diameter), degassed under dynamic vacuum, and sealed. The six ampoules were heated from room temperature (RT) to 225 °C within 3 h and maintained at that temperature for 24 h. Subsequently, the temperature increased from 225 °C to 440 °C within 5 h, remaining below the melting temperature of SbSeI ~452 °C [30]. The samples were held at 440 °C for 256 h, followed by natural cooling in air to RT (Fig. S1). Additionally, the samples with Bi content x = 0.6, 0.8 and 1 were recrystallized at 480 °C for 472 h to enhance crystallinity and eliminate secondary phases, including Bi_2Se_3 and BiI_3 as identified by X-ray diffraction (XRD) after the initial annealing. The higher recrystallization temperature was selected for Bi-rich (x > 0.5) compositions due to the significantly higher melting point of BiSeI (T_M=545 °C [31]) compared to SbSeI. After the synthesis, shiny, grey microcrystals were formed and settled at the bottom of the ampoules, including larger needle-like crystals.

A high-resolution scanning electron microscope (HR-SEM Zeiss Merlin) was used to examine the morphology of the microcrystals. Two detectors were utilized for this analysis: a high-efficiency in-lens secondary electron detector, which provided high-contrast surface images, and an energy-selective backscattered electron detector, which enabled compositional contrast imaging. HR-SEM Zeiss Merlin equipped with a Bruker Esprit 1.82 energy dispersive X-ray (EDX) system with an EDX-XFlash 3001 detector for compositional analysis of the microcrystals. High-resolution transmission electron microscopy (HR-TEM) images were acquired using a JEOL JEM-2100F transmission electron microscope equipped with a JEOL JED-2300T Dry SDD energy dispersive X-ray (EDX-TEM) unit. The acceleration voltage was set to 200 keV. To characterize the crystal structure and phase composition of the $Sb_{1-x}Bi_xSeI$ solid solutions, XRD was performed using a Rigaku Ultima IV diffractometer. The diffractometer was operated at 40 kV and 40 mA with monochromatic Cu Kα radiation (λ = 1.5406 Å) detected by a silicon strip detector (D/teX Ultra). Phase analysis and lattice parameters were calculated using the PDXL2 Rigaku software. To further investigate the phase composition of microcrystals, room-temperature micro-Raman (RT μ-Raman) spectroscopy was employed. Raman spectra were collected using a 532 nm laser with a power intensity of 0.42 mW and a spot size of 10–20 μm in diameter on a Horiba LabRam HR 800 spectrometer equipped with a multichannel CCD detection system in a backscattering configuration. The same equipment was used to measure room temperature micro-photoluminescence (RT-PL) in the visible spectral range. The optical band gaps of the materials were determined by analyzing the ultraviolet–visible-near-infrared (UV–Vis–NIR) diffuse reflectance data measured by a Shimadzu UV-3600 two-beam spectrometer equipped with a multi-purpose compartment MPC-3100 with an integrating sphere of the diameter of 60 mm. Measurements were recorded between 260 and 2600 nm. The X-ray photoelectron spectroscopy (XPS) measurements were performed using a Kratos Ultra DLD setup in ultrahigh vacuum conditions, with the base pressure of 10^{-9} mbar, with a monochromatized Al Kα anode, having an energy of 1486.6 eV. The surface charging effects were compensated by using both an electron flood gun during measurement as well as ulterior correction to the C-C contamination bond at 284.6 eV. Ultraviolet photoelectron spectroscopy (UPS) was performed using an Axis Ultra DLD photoelectron spectrometer (Kratos Analytical) equipped with a helium discharge lamp. The He(I) resonance line (hν = 21.21 eV) was used to obtain UPS spectra, allowing the determination of the work function and valence band maximum energies of the materials. An ambient Scanning Kelvin Probe system (SKP5050, KP Technology Ltd, UK) equipped with a 2 mm gold-covered vibrating tip was used to evaluate the photosensitivity and conductivity type of all six materials. A semiconductor red laser with a wavelength of 670 nm and a power of 1 mW was employed to observe changes in surface potential with illumination.

3. Results and discussion

3.1. Characterization of the morphology and composition of $Sb_{1-x}Bi_xSeI$ (x = 0–1) microcrystals

The morphology of the synthesized materials was examined using SEM. Fig. 1 presents top-view SEM images of $Sb_{1-x}Bi_xSeI$ (x = 0–1) microcrystals, revealing structures consisting predominantly of cylindrical or prismatic, needle-shape crystals of varying sizes. The crystals range in length from several tenths of a micrometer to over a millimeter, with diameters ranging from 10 μm to several hundred micrometers. These findings align with previous studies [32], based on the growth

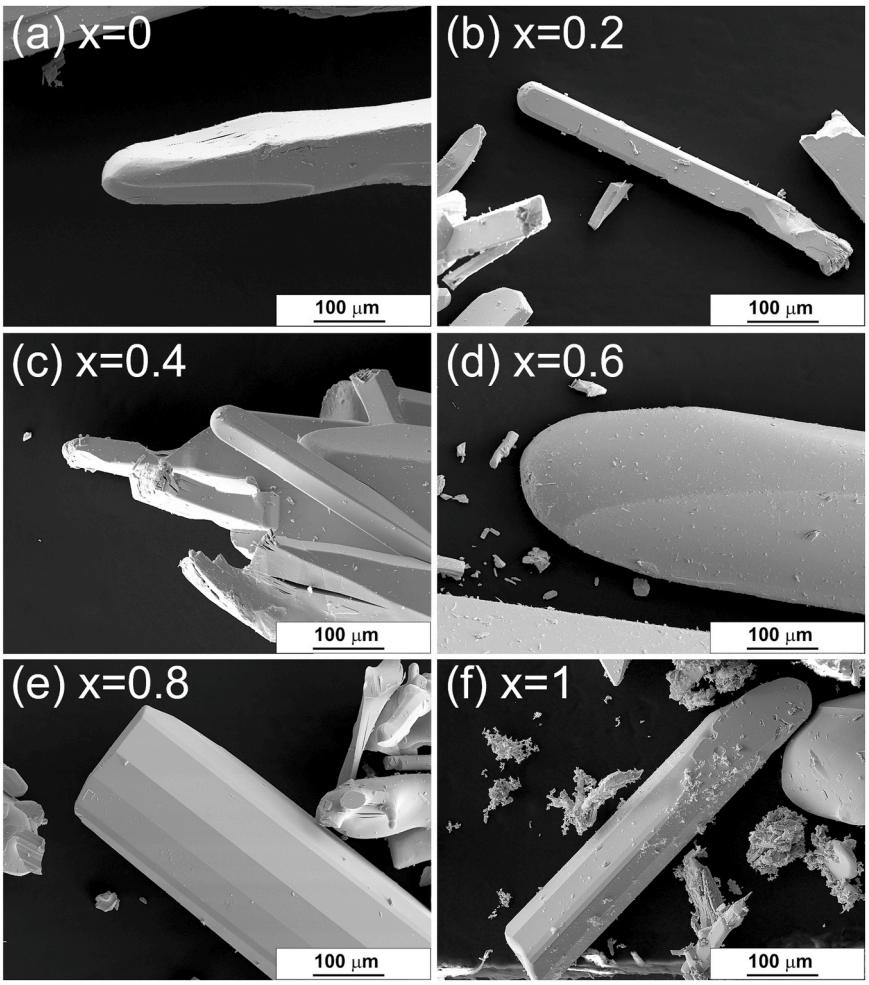

Fig. 1. SEM images of microcrystals of $Sb_{1-x}Bi_xSeI$ (x = 0–1).

mechanism of $A^VB^{VI}C^{VII}$ crystals, where needle-shape structures exhibit a faster growth rate along the *b*-axis. A closer examination revealed that these needles consist of multiple parallel-aligned layers connected along the *a*-axis. In addition, clusters of smaller, irregularly shaped crystals partially covered with nanometer-sized crystals (see Fig. 1f) were observed. Incorporating Bi into the solid solutions resulted in more rounded needle-shaped crystals with a greater number of facets (x = 0.8, 1).

For the elemental compositional analysis of the $Sb_{1-x}Bi_xSeI$ compounds, the samples were embedded in epoxy resin and polished for cross-sectional examination of the crystal's bulk. EDX measurements were performed across multiple regions and crystals within each sample (Fig. S2), revealing consistent elemental distributions that confirmed high compositional uniformity. According to the EDX data (shown in Table 1), the target elemental composition (SbBi = 33.33 %, Se = 33.33 %, I = 33.33 %) was closely achieved throughout the entire series and the substitution of Sb by Bi was confirmed.

Raman spectra of $Sb_{1-x}Bi_xSeI$ solid solutions were measured from single microcrystals and are presented in Fig. 2.

The Raman spectra of $Sb_{1-x}Bi_xSeI$ crystals were fitted using Lorentzian functions, and the corresponding peaks, displayed in different colors, are shown in Fig. 2. The Raman spectra of SbSeI and BiSeI are consistent with previous reports, exhibiting the highest frequency modes at 182 cm^{-1} ($\Gamma_{1(Bi)}$) and 209 cm^{-1} ($\Gamma_{1(Sb)}$), corresponding to the Bi-Se and Sb-Se bonds, respectively, which is in good agreement with [33,34]. Additionally, peaks at 95, 115, 137, 167, 187 and 213 cm^{-1} were identified and attributed to SbSeI. For BiSeI, peaks at 75, 96, 106, 115, 137, 153, 159, 182 and 186 cm^{-1} were observed, aligning well with previous reports [28,35,36]. Peaks at lower wavenumbers (75 and 96 cm^{-1}) are attributed to Bi-I bonds and those at 153, 159, 182, 186 cm^{-1} to Bi-Se bonds. The cationic substitution of Sb with Bi in the $Sb_{1-x}Bi_xSeI$ microcrystals clearly influences the Raman modes. Variations in the Bi content in $Sb_{1-x}Bi_xSeI$ resulted in changes in the relative intensities of the $\Gamma_{1(Bi)}$ and $\Gamma_{1(Sb)}$ vibrational modes. The presence of two distinct modes, rather than a single average mode, in the solid solutions of x = 0.2–0.8 indicates Raman bimodal behavior, similar to that observed in the $Bi_{1-x}Sb_xSI$ system [24] and as reported for $Sb_{0.5}Bi_{0.5}SeI$ [25]. As the Bi content increases, the relative intensities of the two main

Table 1
Elemental composition of $Sb_{1-x}Bi_xSeI$ (x = 0–1) determined by EDX.

$Sb_{1-x}Bi_xSeI$	x = Bi/(Sb+Bi) outcome	Sb (at%)	Bi (at%)	Se (at%)	I (at%)
SbSeI	0	34.1 ± 0.7	-	32.6 ± 0.4	33.3 ± 0.4
$Sb_{0.8}Bi_{0.2}SeI$	0.20	27.0 ± 0.5	6.7 ± 0.1	32.7 ± 0.4	33.6 ± 0.5
$Sb_{0.6}Bi_{0.4}SeI$	0.40	20.5 ± 0.5	13.7 ± 0.3	31.3 ± 0.4	34.5 ± 0.5
$Sb_{0.4}Bi_{0.6}SeI$	0.62	13.0 ± 0.3	21.1 ± 0.5	32.3 ± 0.4	33.6 ± 0.5
$Sb_{0.2}Bi_{0.8}SeI$	0.81	6.6 ± 0.2	27.4 ± 0.6	32.5 ± 0.4	33.4 ± 0.5
BiSeI	1	-	34.2 ± 0.5	32.6 ± 0.3	33.2 ± 0.3

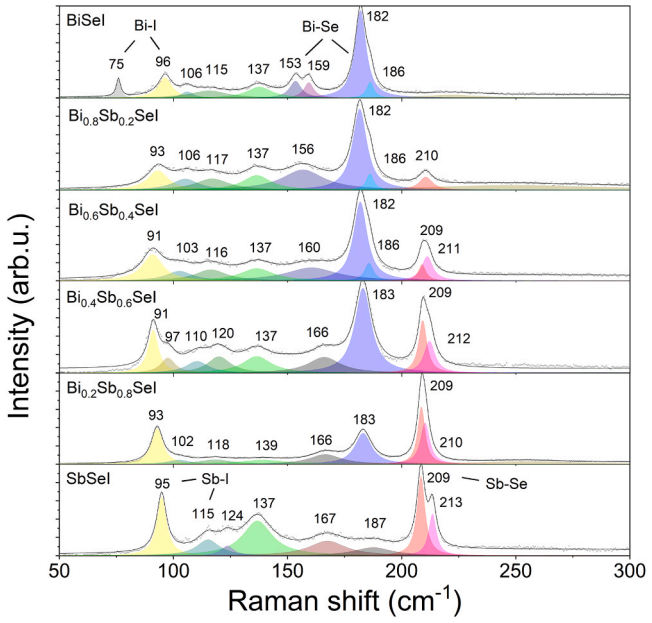

Fig. 2. Normalized Raman spectra of $Sb_{1-x}Bi_xSeI$ (x = 0–1) microcrystals (dots). Fitted spectra (black line) using Lorentzian functions.

peaks of SbSeI and BiSeI change (see Fig. 3), allowing the estimation of the content of metal atoms in the solid solution with relatively high accuracy by Raman spectroscopy. To verify that microcrystal orientation does not affect the Raman measurements, a polarization-dependent study was conducted by varying the microcrystal alignment relative to incident polarized laser. The relative intensities of the Bi–Se and Sb–Se peaks remained constant, confirming the polarization independence of the measurements (Fig. S3).

XRD patterns of $Sb_{1-x}Bi_xSeI$ were recorded and are presented in Fig. 4a. The reflections obtained were compared with data cards of SbSeI (ICSD # 01–076–1354), BiSeI (ICSD # 01–070–4693), $Sb_{0.7}Bi_{0.3}SeI$ (ICDD # 00–065–0522), and $Sb_{0.3}Bi_{0.7}SeI$ (ICDD # 00–066–0065). All peaks align with their expected positions. The position of the reflections gradually shifted to lower angles as the Bi content in the solid solutions increased. For example, the diffraction peak belonging to the reflection of 112 shifted from 29.4° to 28.9° (Fig. 4b). A similar behaviour was also observed for $BiSBr_{1-x}I_x$ solid solutions [37].

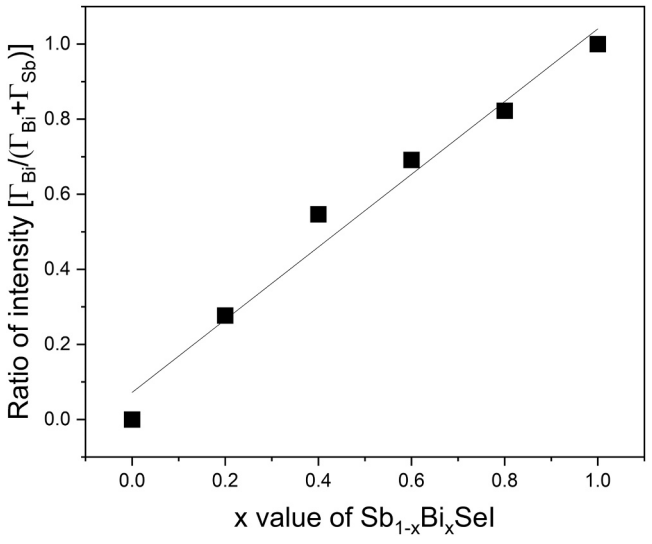

Fig. 3. Ratio of the intensities of the main Raman peaks corresponding to the Sb-Se (209 cm^{-1}) and Bi-Se (182 cm^{-1}) modes.

The lattice parameters for all materials were calculated and presented in Fig. S4. The orthorhombic space group *Pnma* was identified for BiSeI, SbSeI and all intermediate solid solutions. A 3.4 % increase in unit cell volume was observed upon full substitution of Sb with Bi, consistent with the larger atomic radius of Bi compared to Sb and is in good agreement with previous studies [14,19,25]. The expansion is anisotropic: the unit cell parameters *b* and *c* increase with higher Bi content, while the parameter *a* remains nearly constant (see Fig. S4). Both parameters *a* and *b* follow the Vegard's law, exhibiting a linear dependence on Bi content.

The morphology, crystal structure and elemental composition of solid solutions were also characterized by HR-TEM, TEM-EDX and XPS (Table S1).

From the morphological perspective, all samples exhibit large microcrystals (Fig. 5a) that tend to be elongated and have straight edges (facets), formed by specific crystallographic planes. The HR-TEM image reveals that the ribbons align along the long axis of the rods (Fig. 5b). A magnified image of the area shown in Fig. 6b demonstrates a continuous crystalline layer without visible grain boundaries or structural defects such as dislocations (Fig. 5c). The diffraction points indicated in Fig. 5d correspond to the following lattice planes and interplanar distances: (010) – 4.22 Å, (11−1) –3.57 Å, (10−1)-6.72 Å. The orientation of the crystallite is such that the zone axis [101] is parallel to the electron beam for x = 0.8. The selected area diffraction (SAED) pattern revealed a single set of diffraction spots for all solid solutions, confirming their high crystallinity. Fig. 5d illustrates the lattice planes corresponding to $Sb_{1-x}Bi_xSeI$ with x = 0.8.

An orthorhombic crystal structure with *Pnma* space group was found for all solid solutions by SAED, in agreement with XRD results. The lattice parameters of the $Sb_{1-x}Bi_xSeI$ powders with x = 0.2, 0.4, 0.6 and 0.8 were determined using SAED and compared to XRD (Fig. S4). While the SAED measurements provided detailed structural information from individual single crystals, slight discrepancies were observed with XRD results. These differences arise from the fact that SAED was conducted on microcrystals, whereas XRD data were obtained from ground powder samples.

TEM-EDX analysis has been done on microcrystals from solid solutions. The EDX maps reveal that all elements are homogeneously distributed in the areas analysed (Fig. 6). The TEM-EDX results are consistent with the expected stoichiometric ratio ((Bi,Sb):Se:I = 1:1:1) and agree with the SEM-EDX results (Table S1). However, discrepancies between SEM and TEM measurements emerge as the Bi molar fraction increases. Specifically, the Bi content measured by TEM-EDX is higher than that measured by SEM-EDX. This discrepancy can be attributed to the differences in acceleration voltage: 20 keV for SEM-EDX and 200 keV for TEM-EDX. The higher sensitivity of SEM-EDX at 2.3 keV (Bi M line) compared to TEM-EDX can explain the variation in Bi content. Consequently, SEM-EDX results are considered more reliable because of their greater sensitivity in this energy range. The elemental composition of the solid solutions was also investigated by X-ray photoelectron spectroscopy measurements. The XPS results are included in Table S1 for comparison. As expected, some discrepancies arise between EDX and XPS data due to the fundamentally different probing depths of the techniques - EDX being bulk-sensitive, while XPS probes only the top ~5–10 nm of the surface. Moreover, the quantitative interpretation of XPS data is limited by several factors, including surface geometry, peak intensity, the reliability of relative sensitivity factors, surface volume homogeneity, and potential sample degradation during analysis. Additional challenges arise from the heterogeneous nature of the polycrystalline samples, variations in surface composition, and possible contamination [38]. Despite these limitations, the XPS data qualitatively confirms the presence of all constituent elements and shows reasonable agreement with the stoichiometric trends observed by EDX. These results support the overall elemental composition and confirm the consistency of the solid solution series.

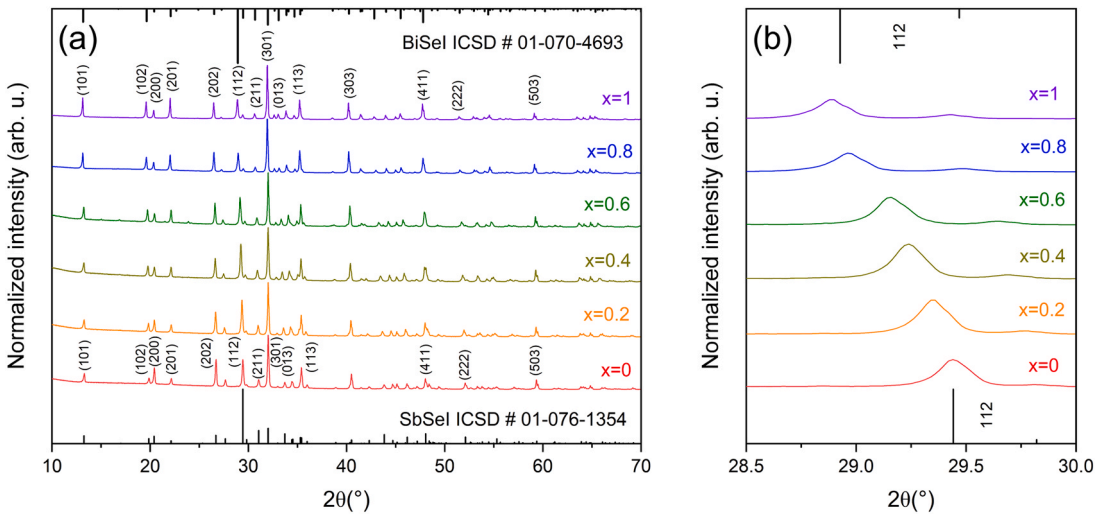

Fig. 4. (a) XRD pattern of $Sb_{1-x}Bi_xSeI$ (x = 0–1) powders. (b) The enlarged XRD pattern shows a shift of the distance between (112) planes.

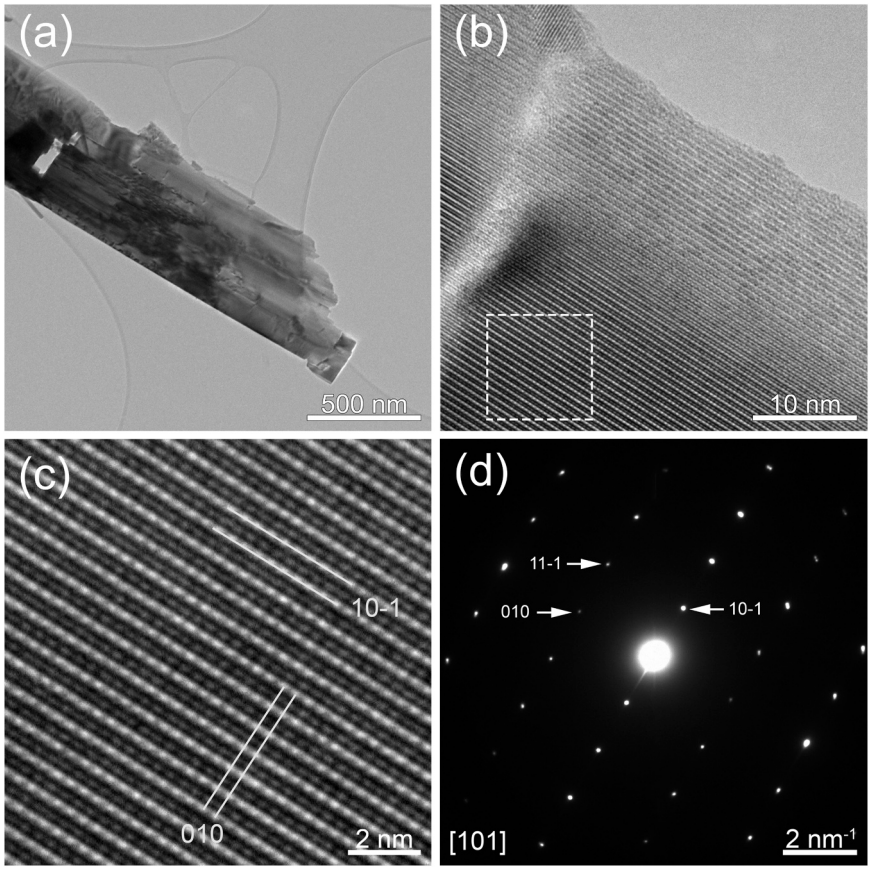

Fig. 5. (a) Low maginification TEM image, (b) HR-TEM image indicating the area that was magnified in (c) where the lattice planes (10−1) and (010) were illustrated and (d) SAED corresponding to $Sb_{1-x}Bi_xSeI$ with x = 0.8.

3.2. Characterization of optical properties of $Sb_{1-x}Bi_xSeI$ (x = 0–1) microcrystals

RT photoluminescence analysis revealed a single, asymmetric emission peak for all solid solutions, as shown in Fig. 7. The observed band shape is characteristic of band-to-band recombination, where the high energy side is mainly determined by the Fermi distribution, while low energy side reflects the density of states function. A more detailed discussion of this shape is provided in [12]. The peak maxima, determined by fitting the spectra with Split Pseudo-Voigt functions, shifted non-linearly from 1.75 eV for SbSeI to 1.41 eV for BiSeI. These values are consistent with previously reported optical band gap energies for SbSeI [11] and BiSeI [12].

UV-Vis-NIR diffuse reflectance spectroscopy was conducted on the samples in the form of a pressed microcrystalline powder, following the methodology described in [12]. The diffuse reflectance data were analyzed using the Kubelka-Munk function (Eq. 1) to determine the optical band gaps of the solid solutions,

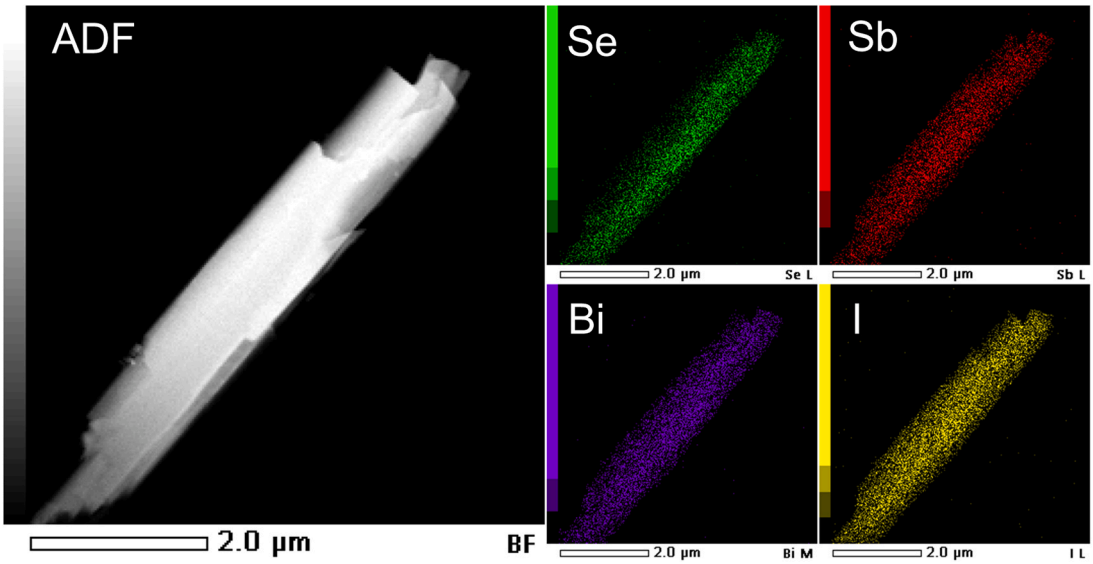

Fig. 6. Dark-field STEM image and EDX elemental mapping (x = 0.4).

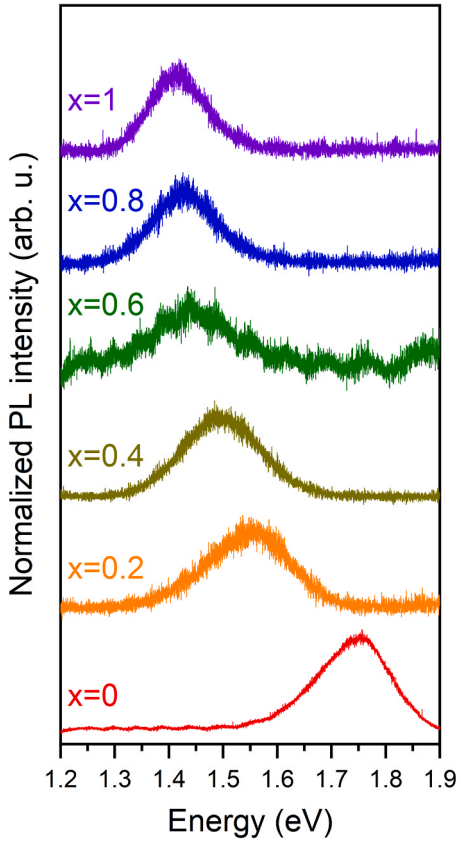

Fig. 7. Room temperature photoluminescence spectra of $Sb_{1-x}Bi_xSeI$ (x = 0–1) microcrystals.

$$F(R_\infty) = \frac{(1-R_\infty)^2}{2R_\infty} \sim \alpha, \tag{1}$$

where R_∞ is the absolute diffuse reflectance. For optically thick samples, $F(R_\infty)$ can be approximated as the absorption coefficient α. When plotted against the photon energy, this function enables for band gap determination by identifying linear regions that intersect the energy axis (see Fig. 8). The optical band gaps were extracted using the Tauc

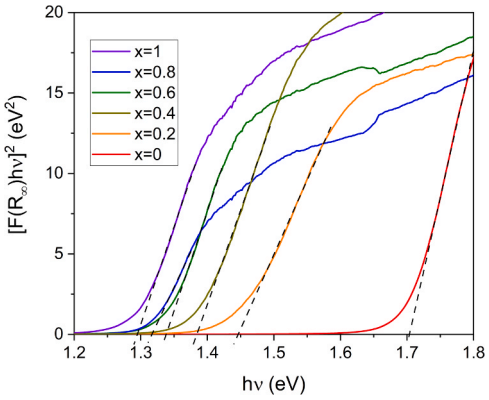

Fig. 8. Optical band gap determination from Tauc plots: extrapolation of the linear least squares fit of $[F(R_\infty)h\upsilon]^2$ vs hυ for $Sb_{1-x}Bi_xSeI$ (x = 0–1) microcrystals.

relation:

$$(F(R_\infty)h\nu)^{1/n} = A(h\nu - E_g), \tag{2}$$

where A is a constant, h the Planck's constant, ν the photon frequency and E_g is the optical band gap. The value of factor n is ½ for direct transitions and 2 for indirect transitions. Band gaps of all solid solutions were estimated using n = ½, assuming the presence of direct band gaps.

The optical band gap of $Sb_{1-x}Bi_xSeI$ solid solutions can be precisely tuned by adjusting the Bi/Sb ratio. The experimentally measured band gap values range from 1.7 eV for SbSeI to 1.29 eV for BiSeI (Fig. 8) are in good agreement with previously reported values 1.72 eV [11] and 1.29 eV [35,39], respectively. In an earlier study, an almost linear decrease of E_g was detected with increasing x value [26]. In contrast, our samples exhibit a nonlinear decrease in band gap with increasing Bi content, as shown in Fig. 9, indicating a characteristic band gap bowing effect. Similar nonlinear behaviour has been reported in other chalcohalide solid solutions, such as $Bi_{1-x}Sb_xSI$ [24], as well as in $Sb_2(S_xSe_{1-x})_3$ [40] or $Ag_xCu_{1-x}GaSe_2$ [41]. This nonlinear behaviour is often attributed to local structural distortions upon substitution, including atom displacements, clustering, or localized states in the band gap. It can also arise from increased spin–orbit coupling when heavier atoms (Bi) replace lighter (Sb) ones. The optical bowing effect in semiconductor

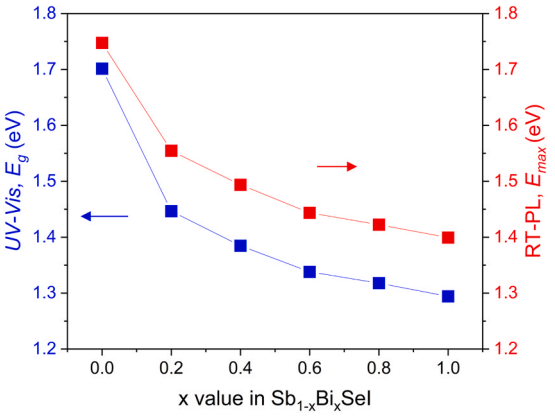

Fig. 9. Optical band gap values (blue squares) along with the maximum emission energy (E_{max}) from photoluminescence spectra (red squares) for $Sb_{1-x}Bi_xSeI$ (x = 0–1) microcrystals as a function of the Bi/Sb ratio.

alloys is linked to differences in atomic electronegativities and internal structural relaxation - specifically, changes in bond lengths and angles [24,40].

Fig. 9 shows the optical band gap values and RT- PL peak energies (E_{max}) as a function of the Bi/Sb ratio in $Sb_{1-x}Bi_xSeI$ (x = 0–1). A similar nonlinear trend is observed for both parameters. In SbSeI, the PL peak energy is only 0.05 eV above the band gap, whereas Bi incorporation leads to a consistent offset, with the PL emission remaining approximately 0.11 eV higher than the direct band gap across all Bi-containing compositions. This behaviour, previously reported for BiSeI [12], is commonly observed in different semiconductors [42,43].

To investigate the impact of Bi incorporation on the band structure of $Sb_{1-x}Bi_xSeI$, a UPS study was conducted across the entire series. Selected microcrystals from each solid solution were analyzed.

The work function (Φ) of the $Sb_{1-x}Bi_xSeI$ compounds was determined from the secondary-electron cutoff energy obtained in UPS measurements using He(I) excitation, as described by Eq. (3)

$$\Phi = h\nu - E_{cutoff} \quad (3)$$

where Φ is the work function, $h\nu$ represents the excitation energy of the He(I) line (21.21 eV), and E_{cutoff} corresponds to the secondary-electron cutoff energy, marking the end of secondary-electron emission at the high binding energy side of the spectrum (Fig. 10a). The work function is defined as the minimum energy required to remove an electron from the Fermi level (E_F) to the vacuum level (E_{VAC}) [44].

The valence band edge (E_{VBM}) was determined from the UPS spectrum in binding energy scale by linearly extrapolating the intersection of the low-binding-energy onset to the baseline (Fig. 10b). Here, E_{VBM} denotes the energy difference between the valence band maximum and the E_F. Combined with the optical band gap values obtained from UV–VIS–NIR measurements, these data were used to estimate the

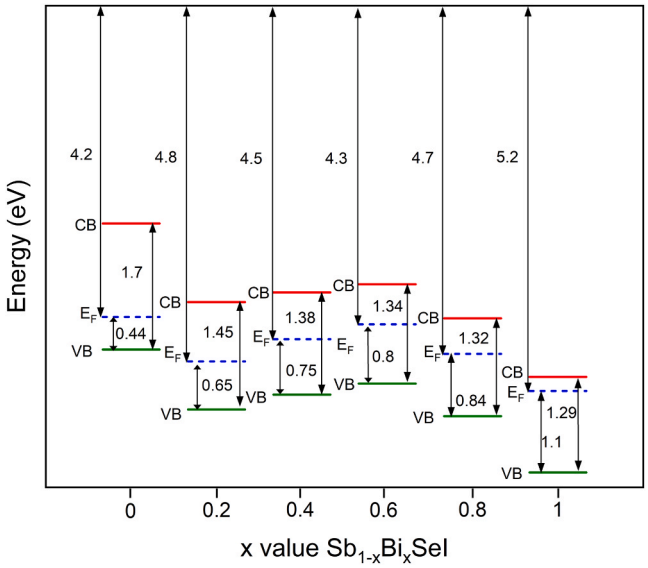

Fig. 11. Experimentally determined band diagram of $Sb_{1-x}Bi_xSeI$ (x = 0–1) solid solutions, illustrating the compositional dependence of work function, valence band edge, and band gap energy.

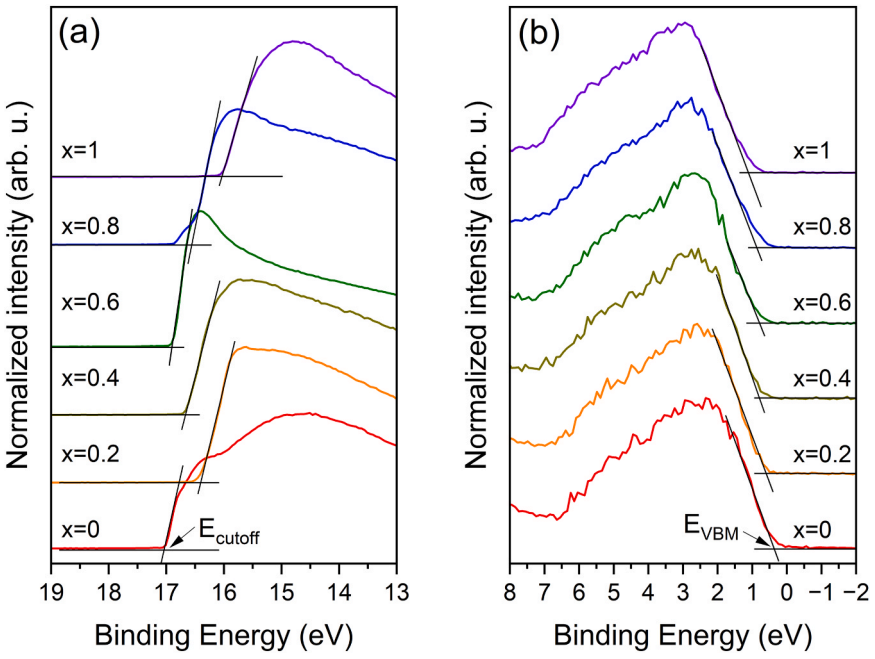

Fig. 10. Ultraviolet photoelectron spectra (UPS) of $Sb_{1-x}Bi_xSeI$ (x = 0–1) shown in the binding energy scale. (a) High binding energy region highlighting the secondary electron cutoff (E_{cutoff}). (b) Low binding energy region showing the valence band onset used to determine the valence band edge (E_{VBM}).

position of the valence band relative to the vacuum level and to construct the experimental energy band diagram of the $Sb_{1-x}Bi_xSeI$ system (Fig. 11).

The UPS study showed that increasing the Bi content in $Sb_{1-x}Bi_xSeI$ shifted the E_{VBM} from 0.44 eV to 1.1 eV, indicating a movement of the Fermi level toward the conduction band. Similar shift in E_{VBM} has been reported in other solid solution systems, such as CZT(S,Se) [45]. A transition in conductivity type from *p*-type to *n*-type was observed when the Bi content exceeded 0.2 (x = 0.2), see Table S2. Despite reports of *n*-type conductivity for SbSeI in the literature, the present findings suggest that the conductivity type is strongly influenced by composition. Comparable work function and band gap values are reported in [20], although the obtained E_{VBM} is considerably lower in that study. Although experimental data for BiSeI are limited, the theoretical studies predict a comparable band gap (1.29 eV) and E_{VBM}, differing by only 0.1 eV from the values determined in this work [14]. Scanning Kelvin Probe measurements performed on all six solid solutions revealed a clear photosensitive response under red laser illumination. For Sb-rich compositions (x = 0, 0.2, 0.4), the contact potential difference (CPD) increased upon illumination, whereas a decrease in CPD was observed for Bi-rich compositions (x = 0.6, 0.8, 1) (Fig. S5). This contrasting behaviour indicates a possible transition in conductivity type from *p*-type to *n*-type as the Bi content surpasses that of Sb, consistent with the findings from UPS analysis.

4. Conclusions

Solid solutions of $Sb_{1-x}Bi_xSeI$ (x = 0–1) have successfully synthesized from Sb_2Se_3, Bi_2Se_3, SbI_3 and BiI_3 precursors, forming microcrystals with needle-shape structures. EDX analysis confirmed the progressive substitution of Sb by Bi across the series. The formation of predominantly single phase of $Sb_{1-x}Bi_xSeI$ solid solutions was confirmed by RT-Raman spectroscopy and XRD, which revealed an orthorhombic crystal structure (*Pnma*) for all compositions. The relative intensity changes in Sb-Se and Bi-Se Raman modes correlated with Bi content in $Sb_{1-x}Bi_xSeI$, offering a spectroscopic indicator of composition. Optical characterization demonstrated that increasing Bi incorporation reduced nonlinearly the band gap from 1.7 eV (SbSeI) to 1.29 eV (BiSeI), positioning the material within the optimal energy range for photovoltaic absorbers. RT-PL exhibited a nonlinear shift in peak emission energy (E_{max}), from 1.75 eV to 1.41 eV across the series. UPS revealed a downward shift in E_{VBM} with higher Bi content, accompanied by a transition from *p*-type to *n*-type conductivity as indicated by both UPS and Scanning Kelvin Probe measurements. These findings highlight the tunable optoelectronic properties of $Sb_{1-x}Bi_xSeI$, underscoring their potential in diverse photovoltaic applications. In particular, the composition $Sb_{0.4}Bi_{0.6}SeI$ with $E_g = 1.34$ eV, is well suited for use as an absorber layer in single junction solar cells. Conversely, SbSeI, with its higher band gap, is a promising candidate for indoor photovoltaic devices or as top absorber in tandem solar cell architecture.

CRediT authorship contribution statement

Maarja Grossberg-Kuusk: Funding acquisition, Writing – review & editing. **Marit Kauk-Kuusik:** Writing – review & editing, Supervision, Project administration, Funding acquisition. **Cristian Radu:** Investigation, Formal analysis. **Aurelian Catalin Galca:** Investigation, Formal analysis. **Amelia Elena Bocirnea:** Formal analysis, Investigation. **Marc Dolcet Sadurni:** Writing – original draft, Methodology, Investigation, Formal analysis, Data curation. **Kristi Timmo:** Writing – review & editing, Supervision, Project administration, Investigation, Formal analysis, Data curation. **Mati Danilson:** Investigation, Formal analysis. **Artūras Suchodolskis:** Investigation, Formal analysis. **Valdek Mikli:** Investigation, Formal analysis. **Jüri Krustok:** Writing – review & editing, Investigation, Formal analysis.

Declaration of Competing Interest

The authors declare that they have no known competing financial interests or personal relationships that could have appeared to influence the work reported in this paper.

Acknowledgements

This work was supported by European Union through the European Regional Development Fund, Project TK210, and by the Estonian Research Council grant PRG1023. NIMP authors acknowledge funding from *Autoritatea Națională pentru Cercetare* (Romanian National Authority for Research) through the Core Programme PC3-PN23080303 project, and from *Unitatea Executivă pentru Finanțarea ÎnvățământuluiSuperior, a Cercetării, Dezvoltării și Inovării* (UEFISCDI) through ERANET-M-3-ERANET-Ligthcell (Contract No. 19/15.03.2024) project. The XPS measurements were performed using the Romanian National Interest Setup "System of complex XPS/ESCA installations and research using synchrotron radiation".

Appendix A. Supporting information

Supplementary data associated with this article can be found in the online version at doi:10.1016/j.jallcom.2025.182292.

References

[1] E. Fatuzzo, G. Harbeke, W.J. Merz, R. Nitsche, H. Roetschi, W. Ruppel, Ferroelectricity in SbSI, Phys. Rev. 127 (1962) 2036–2037, https://doi.org/10.1103/PhysRev.127.2036.
[2] R.E. Brandt, J.R. Poindexter, P. Gorai, R.C. Kurchin, R.L.Z. Hoye, L. Nienhaus, M. W.B. Wilson, J.A. Polizzotti, R. Sereika, R. Žaltauskas, L.C. Lee, J.L. Macmanus-Driscoll, M. Bawendi, V. Stevanović, T. Buonassisi, Searching for "defect-Tolerant" photovoltaic materials: combined theoretical and experimental screening, Chem. Mater. 29 (2017) 4667–4674, https://doi.org/10.1021/acs.chemmater.6b05496.
[3] T. Kobayashi, R. Nishikubo, Y. Chen, K. Marumoto, A. Saeki, Wavelength-recognizable SbSI:Sb_2S_3 photovoltaic devices: elucidation of the mechanism and modulation of their characteristics, Adv. Funct. Mater. 34 (2024) 1–10, https://doi.org/10.1002/adfm.202311794.
[4] I. Caño, J.W. Turnley, P. Benítez, C. López-Álvarez, J.M. Asensi, D. Payno, J. Puigdollers, M. Placidi, C. Cazorla, R. Agrawal, E. Saucedo, Novel synthesis of semiconductor chalcohalide anti-perovskites by low-temperature molecular precursor ink deposition methodologies, J. Mater. Chem. C Mater. 12 (2024) 3154–3163, https://doi.org/10.1039/d3tc04410f.
[5] R. Nie, S.Il Seok, Efficient antimony-based solar cells by enhanced charge transfer, Small Methods 4 (2020) 1–10, https://doi.org/10.1002/smtd.201900698.
[6] P. Chauhan, J. Singh, A. Kumar, Two-dimensional Janus antimony chalcohalides for efficient energy conversion applications, J. Mater. Chem. A Mater. 12 (2024) 16129–16142, https://doi.org/10.1039/d4ta02974g.
[7] H. Song, S. Hajra, S. Panda, S. Hwang, N. Kim, J. Jo, N. Vittayakorn, K. Mistewicz, H. Joon Kim, Antimony sulfoiodide-based energy harvesting and self-powered temperature detection, Energy Technol. 12 (2024) 1–9, https://doi.org/10.1002/ente.202301125.
[8] P. Govindaraj, K. Venugopal, Intrinsic ultra-low lattice thermal conductivity in orthorhombic BiSI: an excellent thermoelectric material, J. Alloy. Compd. 929 (2022) 167347, https://doi.org/10.1016/j.jallcom.2022.167347.
[9] P. Kumar, W. Wahyudi, A. Sharma, Y. Yuan, G.T. Harrison, M. Gedda, X. Wei, A. El-Labban, S. Ahmad, V. Kumar, V. Tung, T.D. Anthopoulos, Bismuth-based mixed-anion compounds for anode materials in rechargeable batteries, Chem. Commun. 58 (2022) 3354–3357, https://doi.org/10.1039/d1cc06456h.
[10] W. Khan, S. Hussain, J. Minar, S. Azam, Electronic and thermoelectric properties of ternary chalcohalide semiconductors: first principles study, J. Electron. Mater. 47 (2018) 1131–1139, https://doi.org/10.1007/s11664-017-5884-z.
[11] M. Dolcet Sadurni, K. Timmo, V. Mikli, O. Volobujeva, I. Mengü, J. Krustok, M. Grossberg-Kuusk, M. Kauk-Kuusik, Preparation and characterization of SbSeI thin films, J. Sci. Adv. Mater. Devices 9 (2024) 100664, https://doi.org/10.1016/j.jsamd.2023.100664.
[12] M. Dolcet Sadurni, J. Krustok, K. Timmo, V. Mikli, R. Kondrotas, M. Grossberg-Kuusk, M. Kauk-Kuusik, Radiative recombination model for BiSeI microcrystals: unveiling deep defects through photoluminescence, J. Phys. Energy 6 (2024) 045004, https://doi.org/10.1088/2515-7655/ad8377.
[13] K.T. Butler, S. McKechnie, P. Azarhoosh, M. Van Schilfgaarde, D.O. Scanlon, A. Walsh, Quasi-particle electronic band structure and alignment of the V-VI-VII semiconductors SbSI, SbSBr, and SbSeI for solar cells, Appl. Phys. Lett. 108 (2016), https://doi.org/10.1063/1.4943973.
[14] A.M. Ganose, K.T. Butler, A. Walsh, D.O. Scanlon, Relativistic electronic structure and band alignment of BiSI and BiSeI: candidate photovoltaic materials, J. Mater. Chem. A Mater. 4 (2016) 2060–2068, https://doi.org/10.1039/c5ta09612j.

[15] E. Wlaźlak, A. Blachecki, M. Bisztyga-Szklarz, S. Klejna, T. Mazur, K. Mech, K. Pilarczyk, D. Przyczyna, M. Suchecki, P. Zawal, K. Szaciłowski, Heavy pnictogen chalcohalides: the synthesis, structure and properties of these rediscovered semiconductors, Chem. Commun. 54 (2018) 12133–12162, https://doi.org/10.1039/c8cc05149f.
[16] C. López, I. Caño, D. Rovira, P. Benítez, J.M. Asensi, Z. Jehl, J.L. Tamarit, E. Saucedo, C. Cazorla, Machine-learning aided first-principles prediction of earth-abundant pnictogen chalcohalide solid solutions for solar-cell devices, Adv. Funct. Mater. 2406678 (2024) 1–14, https://doi.org/10.1002/adfm.202406678.
[17] R. Nie, M. Hu, A.M. Risqi, Z. Li, S.Il Seok, Efficient and stable antimony selenoiodide solar cells, Adv. Sci. 8 (2021) 1–8, https://doi.org/10.1002/advs.202003172.
[18] K.W. Jung, Y.C. Choi, Compositional engineering of antimony chalcoiodides via a two-step solution process for solar cell applications, ACS Appl. Energy Mater. (2021), https://doi.org/10.1021/acsaem.1c02676.
[19] I. Caño, A. Navarro-Güell, E. Maggi, M. Barrio, J.L. Tamarit, S. Svatek, E. Antolín, S. Yan, E. Barrena, B. Galiana, M. Placidi, J. Puigdollers, E. Saucedo, SbSeI and SbSeBr micro-columnar solar cells by a novel high pressure-based synthesis process, J. Mater. Chem. A Mater. (2023) 17616–17627, https://doi.org/10.1039/d3ta03179a.
[20] Y.C. Choi, K.W. Jung, One-step solution deposition of antimony selenoiodide films via precursor engineering for lead-free solar cell applications, Nanomaterials 11 (2021), https://doi.org/10.3390/nano11123206.
[21] W. Shockley, H.J. Queisser, Detailed balance limit of efficiency of p-n junction solar cells, J. Appl. Phys. 32 (1961) 510–519, https://doi.org/10.1063/1.1736034.
[22] G.K. Grandhi, D. Hardy, M. Krishnaiah, B. Vargas, B. Al-Anesi, M.P. Suryawanshi, D. Solis-Ibarra, F. Gao, R.L.Z. Hoye, P. Vivo, Wide-bandgap perovskite-inspired materials: defect-driven challenges for high-performance optoelectronics, Adv. Funct. Mater. (2023) 2307441, https://doi.org/10.1002/adfm.202307441.
[23] S. Hwang, T. Yasuda, Indoor photovoltaic energy harvesting based on semiconducting π-conjugated polymers and oligomeric materials toward future IoT applications, Polym. J. 55 (2023) 297–316, https://doi.org/10.1038/s41428-022-00727-8.
[24] R.A. Groom, A. Jacobs, M. Cepeda, R. Drummey, S.E. Latturner, Structural and optical properties of Sb-substituted bisi grown from sulfur/iodine flux, Inorg. Chem. 56 (2017) 12362–12368, https://doi.org/10.1021/acs.inorgchem.7b01839.
[25] R. Sereika, R. Žaltauskas, S. Bandaru, F. Liu, A. Čerškus, Two-transition behavior in $Bi_{0.5}Sb_{0.5}SeI$ crystals, J. Phys. Chem. Solids 154 (2021), https://doi.org/10.1016/j.jpcs.2021.110031.
[26] Д П Белоцкий, НВ Гавриленко, ДМ Катеринюк, ЯИ Кушнир, ВФ Лапшин, ИБ Моик, ФотопроводиМость и оптические свойства кристаллов и пленок SbSeI-BiSeI, Неорганические Материалы 9 (7) (1973) 1142–1145.
[27] Л Віскунець, Л Піскач, І Олексеюк, Г Яковлюк, СистеМа SbSeI – BiSeI, Науковий вісник Східноєвропейського національного університету іМені Лесі Українки, ХіМічні науки № 24 (2013) 22–24.
[28] G. Kanchana, D. Arivuoli, Spectroscopic investigation of BiSeI, SbSeI compounds and $BiSbS_xSe_{1-x}I$ solid solutions, Indian J. Eng. Mater. Sci. 8 (2001) 373–376.
[29] A. Audzijonis, L. Žigas, A. Kvedaravičius, R. Žaltauskas, The experimental and theoretical investigation of vibration spectra in ferroelectric semiconductor $SbSBr_xI_{1-x}$ crystals, Phys. B Condens Matter 404 (2009) 3941–3946, https://doi.org/10.1016/j.physb.2009.07.162.
[30] Z.S. Aliev, E.C. Ahmadov, D.M. Babanly, I.R. Amiraslanov, M.B. Babanly, The Bi_2Se_3–Bi_2Te_3–BiI_3 system: synthesis and characterization of the $BiTe_{1-x}Se_xI$ solid solutions, CALPHAD 66 (2019) 4–9, https://doi.org/10.1016/j.calphad.2019.101650.
[31] U. Petasch, H. Go, È.H. Oppermann, È. Das, Untersuchungen zum quasibina È ren System Bi_2Se_3/BiI_3, 624 (1998). https://doi.org/10.1002/(SICI)1521-3749(1998110)624.
[32] A.K. Pathak, M.D. Prasad, S.K. Batabyal, One-dimensional SbSI crystals from Sb, S, and I mixtures in ethylene glycol for solar energy harvesting, Appl. Phys. A Mater. Sci. Process 125 (2019) 1–8, https://doi.org/10.1007/s00339-019-2476-1.
[33] S.K. Balakrishnan, P.C. Parambil, E. Edri, Mechanistic insight into the topotactic transformation of trichalcogenides to chalcohalides, Chem. Mater. 34 (2022) 3468–3478, https://doi.org/10.1021/acs.chemmater.2c00306.
[34] S.K. Balakrishnan, P.C. Parambil, L. Houben, M. Asher, O. Yaffe, E. Edri, Revealing hidden phases and self-healing in antimony trichalcogenides and chalcoiodides, Cell Rep. Phys. Sci. 4 (2023) 101298, https://doi.org/10.1016/j.xcrp.2023.101298.
[35] L. Xu, M. Yang, Q. Lu, Y. Ren, Y. Chen, J. Guo, M. Cai, X. Miao, F. Teng, H. Fan, C. Zhang, X. He, P. Hu, 2D BiSeI nanosheets for broadband self-powered photoelectrochemical photodetector, Phys. Status Solidi Rapid Res. Lett. 18 (2024) 1–9, https://doi.org/10.1002/pssr.202300183.
[36] X. Yan, W.L. Zhen, H.J. Hu, L. Pi, C.J. Zhang, W.K. Zhu, High-performance visible light photodetector based on bisei single crystal, Chin. Phys. Lett. 38 (2021), https://doi.org/10.1088/0256-307X/38/6/068103.
[37] H. Kunioku, M. Higashi, R. Abe, Low-temperature synthesis of bismuth chalcohalides: candidate photovoltaic materials with easily, continuously controllable band gap, Sci. Rep. 6 (2016) 1–7, https://doi.org/10.1038/srep32664.
[38] J.F. Moulder, W.F. Stickle, P.E. Sobol, K.D. Bomben, Handbook of X-ray photoelectron spectroscopy, Perkin-Elmer Corporation, Phys. Electron. Div. (1992).
[39] B. Xiao, M. Zhu, L. Ji, B.Bin Zhang, J. Dong, J. Yu, Q. Sun, W. Jie, Y. Xu, Centimeter size BiSeI crystal grown by physical vapor transport method, J. Cryst. Growth 517 (2019) 7–11, https://doi.org/10.1016/j.jcrysgro.2019.04.003.
[40] E.A. Rueda Pérez, E. Regalado-Pérez, A. Cerdán-Pasarán, R.G. Avilez García, N. R. Mathews, $Sb_2(S_xSe_{1-x})_3$ thin films by electrodeposition: role of deposition potential on the formation of the solid solution and photovoltaic performance via device simulation, Curr. Appl. Phys. 47 (2023) 44–53, https://doi.org/10.1016/j.cap.2022.12.011.
[41] V.V. Rakitin, M.V. Gapanovich, D.S. Lutsenko, V.B. Nazarov, A.V. Stanchik, V. F. Gremenok, A.V. Kabyliatski, Studying the effect of composition on the crystal structure, optical properties, and photogenerated current carriers lifetimes in $Ag_xCu_{1-x}GaSe_2$ ($0 \leq x \leq 1$) solid solutions, High. Energy Chem. 58 (2024) 492–498, https://doi.org/10.1134/S0018143924700474.
[42] G. Martinez, B.A. Piot, M. Hakl, M. Potemski, Y.S. Hor, A. Materna, S.G. Strzelecka, A. Hruban, O. Caha, J. Novák, A. Dubroka, Drašar, M. Orlita, Determination of the energy band gap of Bi_2Se_3, Sci. Rep. 7 (2017) 1–5, https://doi.org/10.1038/s41598-017-07211-x.
[43] M. Lang, C. Zimmermann, C. Krämmer, T. Renz, C. Huber, H. Kalt, M. Hetterich, Luminescence properties of $Cu_2ZnSn(S,Se)_4$ solar cell absorbers: state filling versus screening of electrostatic potential fluctuations, Phys. Rev. B 95 (2017) 1–9, https://doi.org/10.1103/PhysRevB.95.155202.
[44] J.W. Kim, A. Kim, Absolute work function measurement by using photoelectron spectroscopy, Curr. Appl. Phys. 31 (2021) 52–59, https://doi.org/10.1016/j.cap.2021.07.018.
[45] T. Olar, I. Lauermann, H. Xie, M. Neuschitzer, E. Saucedo, W. Calvet, A. Steigert, B. Ümsür, B. Chacko, V. Parvan, M. Gorgoi, B. Senkovskiy, M.C. Lux-Steiner, Assessment of chemical and electronic surface properties of the $Cu_2ZnSn(SSe)_4$ after different etching procedures by synchrotron-based spectroscopies, Energy Procedia 84 (2015) 8–16, https://doi.org/10.1016/j.egypro.2015.12.289.